

## Thermo-hydraulic performance analysis of Fe<sub>3</sub>O<sub>4</sub>-water nanofluid-based flat-plate solar collectors

Shafiq, Mehak; Farooq, Muhammad; Javed, Waqas; Loumakis, George; McGlinchey, Don

*Published in:*  
Sustainability

*DOI:*  
[10.3390/su15064704](https://doi.org/10.3390/su15064704)

*Publication date:*  
2023

*Document Version*  
Publisher's PDF, also known as Version of record

[Link to publication in ResearchOnline](#)

*Citation for published version (Harvard):*  
Shafiq, M, Farooq, M, Javed, W, Loumakis, G & McGlinchey, D 2023, 'Thermo-hydraulic performance analysis of Fe<sub>3</sub>O<sub>4</sub>-water nanofluid-based flat-plate solar collectors', *Sustainability*, vol. 15, no. 6, 4704.  
<https://doi.org/10.3390/su15064704>

### General rights



Copyright and moral rights for the publications made accessible in the public portal are retained by the authors and/or other copyright owners and it is a condition of accessing publications that users recognise and abide by the legal requirements associated with these rights.

### Take down policy

If you believe that this document breaches copyright please view our takedown policy at <https://edshare.gcu.ac.uk/id/eprint/5179> for details of how to contact us.

## Article

# Thermo-Hydraulic Performance Analysis of Fe<sub>3</sub>O<sub>4</sub>-Water Nanofluid-Based Flat-Plate Solar Collectors

Mehak Shafiq <sup>1,\*</sup>, Muhammad Farooq <sup>2</sup> , Waqas Javed <sup>1</sup>, George Loumakis <sup>1</sup>  and Don McGlinchey <sup>1,\*</sup>

<sup>1</sup> School of Computing, Engineering and Built Environment, Glasgow Caledonian University, Glasgow G4 0BA, UK

<sup>2</sup> Department of Mechanical Engineering, University of Engineering and Technology, Lahore 54890, Pakistan

\* Correspondence: mehak.shafiq@gcu.ac.uk (M.S.); d.mcglinchey@gcu.ac.uk (D.M.)

**Abstract:** A cost-effective alternative for lowering carbon emissions from building heating is the use of flat-plate solar collectors (FPSCs). However, low thermal efficiency is a significant barrier to their effective implementation. Favorable nanofluids' thermophysical properties have the potential to increase FPSCs' effectiveness. Accordingly, this study evaluates the performance of an FPSC operating with Fe<sub>3</sub>O<sub>4</sub>-water nanofluid in terms of its thermo-hydraulic characteristics with operating parameters ranging from 303 to 333 K for the collector inlet temperature, 0.0167 to 0.05 kg/s for the mass flow rate, and 0.1 to 2% for nanoparticles' volume fraction, respectively. The numerical findings demonstrated that under identical operating conditions, increasing the volume fraction up to 2% resulted in an improvement of 4.28% and 8.90% in energy and energy efficiency, respectively. However, a 13.51% and 7.93% rise in the friction factor and pressure drop, respectively, have also been observed. As a result, the performance index (PI) criteria were used to determine the optimal volume fraction (0.5%) of Fe<sub>3</sub>O<sub>4</sub> nanoparticles, which enhanced the convective heat transfer, exergy efficiency, and energy efficiency by 12.90%, 4.33%, and 2.64%, respectively.

**Keywords:** Fe<sub>3</sub>O<sub>4</sub>; energy and exergy; flat-plate solar collector; friction factor; pressure drop; performance index



**Citation:** Shafiq, M.; Farooq, M.; Javed, W.; Loumakis, G.; McGlinchey, D. Thermo-Hydraulic Performance Analysis of Fe<sub>3</sub>O<sub>4</sub>-Water Nanofluid-Based Flat-Plate Solar Collectors. *Sustainability* **2023**, *15*, 4704. <https://doi.org/10.3390/su15064704>

Academic Editors: Sylwia Polesek-Karczewska and Izabela Wardach-Święcicka

Received: 6 February 2023

Revised: 1 March 2023

Accepted: 5 March 2023

Published: 7 March 2023



**Copyright:** © 2023 by the authors. Licensee MDPI, Basel, Switzerland. This article is an open access article distributed under the terms and conditions of the Creative Commons Attribution (CC BY) license (<https://creativecommons.org/licenses/by/4.0/>).

## 1. Introduction

Water and space heating account for nearly half of all energy consumption worldwide. According to the International Energy Agency [1], 64% of global energy consumed in buildings for water and space heating is fulfilled by fossil fuels, resulting in a record-breaking 2.5 Gt of direct CO<sub>2</sub> emission. This alarming increase in CO<sub>2</sub> emissions and the corresponding rise in global temperature is one of the world's most pressing challenges today. Therefore, the demand for renewable and sustainable energy has emerged as one of the world's top priorities due to the diminishing supply of fossil fuels and the harm they inflict on the environment.

The abundant supply of solar energy and its minimal environmental impact make it an appealing renewable energy source. Converting solar radiation into usable heat using solar collectors is among the most popular ways of harnessing solar power. The most popular collectors are FPSCs and ETCs, accounting for 93.66% of the global total installed capacity in 2020 [2]. Even though evacuated tube collectors (ETCs) are a mature technology with higher thermal efficiencies, they are relatively expensive. On the other hand, FPSCs benefit from a simple structure, high-pressure bearing, ease of manufacturing and installation, and low maintenance cost. Additionally, they benefit from both diffuse and beam solar radiation, which eliminates the requirement for sun-tracking equipment. These factors make FPSCs a preferred choice for residential, industrial, and commercial buildings. However, they still have some engineering limitations, such as low thermal efficiencies and high thermal losses [3,4]. It may be possible to reduce some of the energy demand and carbon emissions related to heating by increasing the effectiveness of these collectors. To

enhance the efficiency of FPSCs, researchers all over the world have undoubtedly applied a number of techniques, such as modification of geometry or using an efficient solar thermal fluid. In this regard, nanofluids have recently been the subject of active research for enhancing the collector's efficiency.

Nanofluids are primarily a dispersion of different nanometer-sized (1 to 100 nm) particles in traditional solar thermal fluids (e.g., water, oil, ethylene or propylene glycol, etc.). Since the discovery of nanofluids by Choi [5], the research community has been investigating various facets of nanofluids, including their thermophysical characteristics, heat transfer, and rheology. Improved thermal conductivity, a higher surface-to-volume ratio, greater heat transfer, and Brownian motion are some of the specific characteristics of nanofluids that make them an efficient heat transfer fluid [6].

The effectiveness of FPSCs using nanofluids has been the subject of numerous investigations. Experimental research was performed to determine the FPSC's performance using a Cu water nanofluid. Copper (Cu) nanoparticles with mass fractions of 0.1% and 0.2% were utilized to synthesize nanofluid. Compared to traditional water-based FPSCs, the use of Cu nanoparticles (25 nm and 0.1%) raised the overall energy efficiency by 23.83%. Furthermore, the mass fraction and nanoparticle size above 0.1% and 25 nm, respectively, caused agglomeration and increased viscosity, which decreased the collector's efficiency [7]. A CuO water nanofluid was used in FPSC, which resulted in a 21.8% increase in energy efficiency when compared to water at 1 kg/min, which was determined to be an optimum flow rate [8]. Using the finite difference method, a 2D mathematical model was created in MATLAB considering the transient behavior of FPSCs using an Al<sub>2</sub>O<sub>3</sub> water nanofluid. The investigation was performed with varying flow rates from 0.004 kg/s to 0.06 kg/s, and three volume fractions (1%, 2%, and 3%) were used. An increase of 7.2% was obtained in the collector's outlet temperature using three vol% nanoparticles at 0.004 kg/s [9]. The application of WO<sub>3</sub> and CeO<sub>2</sub> in FPSC was investigated experimentally at different values of mass flux. Nanoparticle volume fractions were taken as 0.0167%, 0.0333%, and 0.0666%. The highest gains in collector thermal efficiency over water were 10.75% and 13.48% for CeO<sub>2</sub> and WO<sub>3</sub>, respectively [10,11].

In order to study the impact of covalently functionalized graphene nanoplatelets (GNP) on FPSC's performance, the aqueous nanofluids were prepared with different specific surface areas of GNP and weight fractions of 0.025%, 0.05%, 0.075%, and 0.1%. Among the studied nanofluids, water-based GNP nanofluid with a specific surface area of 750 m<sup>2</sup>/g and 0.1 wt% concentration was reported as the best alternative for efficiency enhancement in FPSCs [12]. An experimental and analytical investigation was performed using silica nanofluid (SiO<sub>2</sub>/deionized water) in FPSC by Jouybari et al. [13] for varied mass flow rates (1, 2, and 3 L/min) and volume fractions (0.4% and 0.6%). Energy efficiency was found to enhance by 1.8% when the particle fraction was raised from 0.4% to 0.6%.

An experimental and numerical investigation using alumina nanofluid (Al<sub>2</sub>O<sub>3</sub>) in an FPSC operating at 5.5 L/min showed an enhancement of 18% in the collector's energy efficiency in comparison to water. The numerical outcomes further demonstrated that Al<sub>2</sub>O<sub>3</sub> nanoparticles were effective in FPSC up to 0.5% volume concentration, but that above this concentration, the thermal efficiency deteriorated [14]. A sensitivity analysis of FPSC's energy efficiency was performed by Tong et al. [15] using Al<sub>2</sub>O<sub>3</sub>, CuO, MWCNT, and Fe<sub>3</sub>O<sub>4</sub> nanofluids at various operating parameters. According to their investigation, FPSCs had the highest efficiency (87%) for MWCNT of all the nanofluids tested, but it was also the most susceptible to changes in operating conditions. The least sensitive material to changes in operating conditions was found to be Fe<sub>3</sub>O<sub>4</sub>.

Thermal or energy analysis alone cannot demonstrate the benefits of employing nanofluids in solar collectors. For the thorough identification of the usefulness of nanofluids, exergy analysis and the pressure drop that occurred in solar collectors are equally important. Exergy is the maximum useful output produced by the system in relation to the temperature difference [16]. Several studies using nanofluids as solar thermal fluids have examined the energy and exergy of FPSCs. An experimental evaluation of an FPSC was performed

using various nanofluids including water-based MgO, Al<sub>2</sub>O<sub>3</sub>, TiO<sub>2</sub>, SiO<sub>2</sub>, CuO, Graphene, and MWCNT. At the optimum values of flow rate and nanoparticle fraction, which were 1.5 L/min and 0.75 vol%, respectively, a MgO water nanofluid exhibited an enhancement in exergy and energy efficiencies of 32.23% and 9.34%, respectively. Additionally, among various nanofluids, the greatest increase in energy and energy efficiency was demonstrated by MWCNT water nanofluid, with respective values of 23.47% and 29.32% [17,18]. Another experimental evaluation of an FPSC using Al<sub>2</sub>O<sub>3</sub> and CuO demonstrated that Al<sub>2</sub>O<sub>3</sub> provided the best collector performance with a 1.0% volume fraction, outperforming water with a 21.9% and 56.9% improvement in energy and exergy efficiencies, respectively [19]. Thermodynamic optimization of an FPSC was conducted by Okonkwo et al. [20] with Al<sub>2</sub>O<sub>3</sub> water and Al<sub>2</sub>O<sub>3</sub>-Fe water nanofluids. The collector's energy efficiency improved by 2.16% for Al<sub>2</sub>O<sub>3</sub> and reduced by 1.7% for Al<sub>2</sub>O<sub>3</sub>-Fe. However, the exergy efficiency was improved for both nanofluids.

The effect of various parameters, including nanoparticle percentage fraction, nanoparticle diameter, Reynolds and Richardson number, on-pressure drop, entropy generation, and heat transfer was investigated using a 3D numerical model (ANSYS Fluent) of an FPSC working with alumina nanofluid [21]. With the increase in nanoparticle fraction or Richardson number, the heat transfer coefficient augmented while entropy generation was reduced. Furthermore, the maximum efficiency was found at a 2% volume fraction. An analytical evaluation of an FPSC was conducted for water and nanofluids, including CuO water, TiO<sub>2</sub> water, MgO water, and Al<sub>2</sub>O<sub>3</sub> water [22]. The ranges for nanoparticle fraction and flow rate were chosen to be 1 to 4% and 1 to 4 L/min, respectively. CuO water demonstrated a higher increase of 38.21% and 14.86% in energy and exergy efficiencies, respectively, among several nanofluids stated above. The study also shows the collector's energy and exergy efficiency can be enhanced by rising the fluid density, volume fraction, and mass flow rate while reducing the specific heat capacity. Theoretical investigations of an FPSC that uses different nanofluids revealed that producing nanofluid-based collectors results in approximately 170 kg fewer CO<sub>2</sub> emissions than traditional water-based FPSCs [23].

The potential of various nanoparticles in FPSCs at different nanoparticle sizes, concentrations, and fluid flow rates have been thoroughly reviewed by several researchers [24–26]. From the findings, it is inferred that nanofluids perform better than traditional solar fluids at enhancing the thermal performance of FPSCs, particularly with smaller sizes and low-volume fractions (below 3%). However, the extent of enhancement in the collector performance and the optimum particle fraction varies, and no unified conclusion can be drawn from the open literature. The majority of research generally ascribed enhanced thermal conductivity of nanofluids to improved solar collector performance; however, nanoparticles also cause fluids to become more viscous, causing additional pressure to drop. Most of the published research has focused mainly on investigating the FPSC's energy and/or exergy efficiencies, while a thorough investigation of the pressure drop resulting from the increased nanofluids viscosity has rarely been reported. Furthermore, the previous numerical studies assumed uniform fluid flow through all risers of the FPSC. However, this might not be the case in practice in this type of arrangement of headers and risers. A numerical approach based on CFD is a useful way of analyzing temperature and flow distribution throughout the headers and risers of FPSCs. By using the average velocity in each riser from the CFD simulation, the pressure drop can be calculated more precisely. Accordingly, this paper presents the formulation of a numerical model of FPSCs in a combined framework of MATLAB and CFD (ANSYS Fluent) to investigate the effect of Fe<sub>3</sub>O<sub>4</sub> water on energy efficiency, exergy efficiency, convection heat transfer, friction factor, and pressure drop of FPSCs. Moreover, the influence of several significant operating parameters, including mass flow rate, nanoparticle volume fraction, and inlet temperature has been thoroughly investigated. Additionally, the usefulness of magnetite nanofluid in FPSCs is assessed using the ratio of efficiency improvement to pressure drop, and the most suitable volume fraction of nanoparticles (Fe<sub>3</sub>O<sub>4</sub>) is determined.

## 2. Theoretical Background

The equations used to determine the thermo-hydraulic characteristics of the FPSCs are described in this section.

- The FPSC operates in a steady-state condition.
- The physical characteristics of insulation, glazing, and absorber plate are temperature independent.
- Both the ambient temperature and solar radiation are constant.
- The nanofluid is taken as a homogenous (single-phase) fluid.
- The variation in mass flow rate in riser tubes (as observed from the CFD model) was within a  $\pm 20\%$  range, which maintained laminar flow conditions. As a result, the flow is regarded as uniform when calculating the heat losses through the collector.

### 2.1. Formulation of Energy and Exergy Efficiencies of FPSC

The useful energy, heat losses, and energy efficiency of an FPSC are formulated according to the model proposed by Hottel and Whillier as described in [27]. In steady-state, Equation (1) presents the energy balance of an FPSC, where  $Q_u$  is the collector's useful energy gain calculated as the difference between the radiation it absorbs and the entire amount of heat loss it experiences through conduction, convection, and radiation.

$$Q_u = A_c (I (\tau\alpha)_e - U_L (T_{pm} - T_a)) \quad (1)$$

where  $(\tau\alpha)_e$  is the optical efficiency, while  $A_c$ ,  $I$ ,  $U_L$ ,  $T_{pm}$ , and  $T_a$  represent the collector's gross area, incident radiation, total heat loss coefficient, absorber plate mean temperature, and ambient temperature, respectively.

To calculate the overall heat loss that occurred in an FPSC,  $U_L$  is estimated by adding the coefficients of heat loss from the top ( $U_t$ ), bottom ( $U_b$ ), and edges ( $U_e$ ) of the collector.

$$U_L = U_t + U_b + U_e \quad (2)$$

The coefficient of heat loss from the top ( $U_t$ ) is calculated by an empirical equation developed by Klein [28].

$$U_t = \left( \frac{N_g}{\frac{C}{T_{pm}} \left[ \frac{T_{pm} - T_a}{N_g + f} \right]^e + h_w} \right)^{-1} + \frac{\sigma (T_{pm} + T_a) (T_{pm}^2 + T_a^2)}{(\varepsilon_p + 0.00591 N_g h_w)^{-1} + \frac{2N_g + f - 1 + 0.133 \varepsilon_p}{\varepsilon_g} - N_g} \quad (3)$$

where  $N_g$  is the quantity of glass covers ( $N_g = 1$  in this study), while  $h_w$ ,  $\sigma$ ,  $\varepsilon_p$ , and  $\varepsilon_g$  are the wind heat transfer coefficient, Stefan–Boltzmann constant, absorber plate emissivity, and glass covers emissivity, respectively.

$C$ ,  $f$ , and  $e$  are determined as:

$$C = 520 \left( 1 - 0.000051 \beta^2 \right) \text{ when } 0^\circ < \beta < 70^\circ \quad (4)$$

and if  $70^\circ < \beta < 90^\circ$ , take  $\beta = 70^\circ$

$$f = \left( 1 + 8.9 \times 10^{-2} h_w - 1.17 \times 10^{-1} h_w \varepsilon_p \right) \left( 1 + 7.87 \times 10^{-2} N_g \right) \quad (5)$$

$$e = 0.430 (1 - 100/T_{pm}) \quad (6)$$

$\beta$  is the collector's tilt angle and  $h_w$  is calculated as [29]:

$$h_w = 5.74 \frac{V_w^{0.8}}{L^{0.2}} \quad (7)$$

where  $v_w$  and  $L$  are the wind speed and collector's length, respectively.

Heat loss coefficients for the bottom ( $U_b$ ) and edges ( $U_e$ ) of the collector are calculated as follows:

$$U_b = \frac{k_{ins,b}}{\delta_{ins,b}} \quad (8)$$

$$U_e = \frac{k_{ins,e}}{\delta_{ins,e}} \cdot \frac{A_e}{A_c} \quad (9)$$

where  $k_{ins,b}$  and  $k_{ins,e}$  refer to the bottom and edge insulation thermal conductivity, respectively. The thicknesses of bottom and edge insulation are represented by  $\delta_{ins,b}$  and  $\delta_{ins,e}$ , respectively. The edge surface area is  $A_e$ .

As indicated in Equation (3),  $U_t$  depends on the absorber plate temperature ( $T_{pm}$ ), which must first be calculated in order to determine  $U_t$  and subsequently  $U_L$ . Therefore,  $T_{pm}$  is calculated as:

$$T_{pm} = T_i + \frac{Q_u}{A_c F_R U_L} (1 - F_R) \quad (10)$$

$$F_R = \frac{\dot{m} C_p}{A_c U_L} \left\{ 1 - \exp\left(-\frac{A_c U_L F'}{\dot{m} C_p}\right) \right\} \quad (11)$$

where  $F_R$  and  $F'$  represent the heat removal factor and efficiency factor.  $F'$  is calculated as:

$$F' = \frac{\frac{1}{U_L}}{W \left[ \frac{1}{U_L(W-D_o)F} + \frac{1}{C_b} + \frac{1}{\pi D_i h_f} \right]} \quad (12)$$

The conductance of the bond ( $C_{bond}$ ) between riser tubes and the absorber plate is defined as:

$$C_{bond} = \frac{kb}{\delta} \quad (13)$$

The width and thickness of the bond are denoted by  $b$  and  $\delta$ , respectively, while  $k$  represents the thermal conductivity of the bond. The factor  $(1/C_b)$  can be ignored in the current analysis assuming a good thermal contact between the riser tubes and the absorber plate, which indicates a very high value for  $C_{bond}$  (i.e.,  $1/C_{bond} = 0$ ) [29].  $D_i$ ,  $D_o$ ,  $h_f$ , and  $W$  are the inner diameter, outer diameter, fluid convective heat transfer coefficient, and the spacing between riser tubes, respectively.  $h_f$  is computed as [30]:

$$h_f = \frac{Nu k_f}{D_i} \quad (14)$$

For the straight rectangular profile, Equation (15) is used to calculate the standard fin efficiency ( $F$ ):

$$F = \frac{\tanh\left(\frac{m(W-D_o)}{2}\right)}{\frac{m(W-D_o)}{2}} \quad (15)$$

with:

$$m = \sqrt{\frac{U_L}{k_p \delta_p}} \quad (16)$$

$\delta_p$  and  $k_p$  representing the absorber plate's thickness and thermal conductivity, respectively.

The following is an empirical correlation to determine the Nusselt number ( $Nu$ ) for the base fluid (pure water), which is valid for uniform heat flux and laminar flow conditions [27]:

$$Nu = 4.4 + \frac{a(Re Pr D_i / L_r)^m}{1 + b(Re Pr D_i / L_r)^n} \quad (17)$$

The constants  $a$ ,  $b$ ,  $m$ , and  $n$  are 0.00236, 0.00857, 1.66, and 1.13, respectively.

For nanofluids, the Nusselt number is estimated employing the following correlation [31]:



$$Nu = 0.4328 \left(1 + 11.285 \phi^{0.754} Pe_{np}^{0.218}\right) Re_{nf}^{0.333} Pr_{nf}^{0.4} : \text{laminar flow } (Re \leq 2300) \quad (18)$$

The dimensionless Reynolds number ( $Re$ ), Prandtl ( $Pr$ ) number, and nanoparticle Peclet number are defined as follows [30,31]:

$$Re = \frac{\rho V_m D_i}{\mu} = \frac{4 \dot{m}_r}{\pi D_i \mu} \quad (19)$$

$$Pr = \frac{\mu C_p}{k} \quad (20)$$

and:

$$Pe_{np} = \frac{V_m d_{np}}{\alpha_{nf}} \quad (21)$$

The mass flow rate and mean fluid velocity of risers are represented by  $\dot{m}_r$  and  $V_m$ , respectively.  $d_{np}$  is the nanoparticle diameter and  $\alpha_{nf}$  refers to the thermal diffusivity of nanofluid, which is given as:

$$\alpha_{nf} = \frac{k_{nf}}{\rho_{nf} C_{p_{nf}}} \quad (22)$$

Finally, energy efficiency ( $\eta_{en}$ ) is given as:

$$\eta_{en} = \frac{Q_u}{A_c I} = \frac{\dot{m} C_p (T_o - T_i)}{A_c I} \quad (23)$$

Moreover, exergy efficiency is calculated by the equation below, which is represented as the collector's useful exergy ( $Ex_u$ ) divided by the incoming solar exergy ( $Ex_{sun}$ ) [20,32].

$$\eta_{ex} = \frac{Ex_u}{Ex_{sun}} \quad (24)$$

The solar exergy flow is calculated as follows [33,34]:

$$Ex_{sun} = A_c I \left[ 1 - \frac{4}{3} \left( \frac{T_a}{T_{sun}} \right) + \frac{1}{3} \left( \frac{T_a}{T_{sun}} \right)^4 \right] \quad (25)$$

The sun's surface temperature ( $T_{sun}$ ) in the above equation is taken as 5778 K.

The collector's useful exergy  $Ex_u$  that takes into account all the irreversibilities caused by the process of heat transfer and pressure drop is given as:

$$Ex_u = \dot{m} C_p \left( T_o - T_i - T_a \ln \frac{T_o}{T_i} \right) - \dot{m} \frac{T_a}{T_{fm}} \frac{\Delta P}{\rho} \quad (26)$$

where  $T_{fm}$  and  $\Delta P$  represent the mean fluid temperature and pressure drop, respectively.

The nanofluid's thermophysical properties are obtained using Equations (27)–(32) [35–37].

Density:

$$\rho_{nf} = (1 - \phi) \rho_{bf} + \phi \rho_{np} \quad (27)$$

Specific heat capacity:

$$C_{p_{nf}} = \frac{(1 - \phi) (\rho C_p)_{bf} + \phi (\rho C_p)_{np}}{\rho_{nf}} \quad (28)$$

Thermal conductivity:

$$k_{nf} = \left( 1 + 4.4 Re_{np}^{0.4} Pr_{bf}^{0.66} \left( \frac{T}{T_{fr}} \right)^{10} \left( \frac{k_{np}}{k_{bf}} \right)^{0.03} \phi^{0.66} \right) k_{bf} \quad (29)$$

where  $Pr_{bf}$  and  $T_{fr}$  represent the base fluid's Prandtl number and freezing point, respectively.  $T$  is the nanofluid temperature ranging between 294 K and 324 K. The particle Reynolds number ( $Re_{np}$ ) is defined as:

$$Re_{np} = \frac{2\rho_{bf}K_B T}{\pi\mu_{bf}^2 d_{np}} \quad (30)$$

Dynamic viscosity:

$$\mu_{nf} = \frac{\mu_{bf}}{1 - 34.87 \left( \frac{d_{np}}{d_{bf}} \right)^{-0.3} \phi^{1.03}} \quad (31)$$

where:

$$d_{bf} = 0.1 \left( \frac{6M}{N\pi\rho_{bf0}} \right)^{1/3} \quad (32)$$

In the above equations,  $\phi$  represents the nanoparticle volume fraction. The validity of dynamic viscosity correlation is  $0.01\% < \phi < 7.1\%$  and  $294 \text{ K} \leq T \leq 333 \text{ K}$ . Where  $d_{bf}$ ,  $M$ ,  $N$ ,  $\rho_{bf0}$ , and  $K_B$  represent the base fluid molecular diameter, molecular weight of water, Avogadro number, base fluid's mass density, and the Boltzmann constant, respectively. The required properties of  $\text{Fe}_3\text{O}_4$  nanoparticles are taken from [15] and temperature-dependent properties of water are taken from reference [38].

## 2.2. Formulation of Pressure Drop in FPSC

The following equation can be used for calculating the pressure drop ( $\Delta P$ ) across the FPSC [39]:

$$\Delta P = \rho g(L_r \sin\beta + h_L) \quad (33)$$

where  $h_L$ , the total head loss, is expressed by [40]:

$$h_L = \sum_j f_j \frac{L_r}{D_i} \frac{v_{mj}^2}{2g} + \sum_j K_{Lj} \frac{v_{mj}^2}{2g} \quad (34)$$

where  $j$  represents each riser tube,  $D_i$  is the inner diameter,  $L_r$  is the riser tube length,  $v_m$  represents mean fluid velocity, and  $f$  is the friction factor, which is estimated as:

$$f = \frac{64}{Re} \quad \text{for laminar flow.} \quad (35)$$

According to [40], the minor loss coefficients ( $K_L$ ) for the entrance and exit tees are taken as 0.5 and 2, respectively, considering the contact between headers and risers is the sharp edge.

The potential of using nanofluid as a solar thermal fluid in FPSCs has been assessed using a performance index (PI), which is expressed as follows [12]:

$$PI = \frac{(\eta_{en})_{nf} / (\eta_{en})_{bf}}{(\Delta P)_{nf} / (\Delta P)_{bf}} \quad (36)$$

It appears that an effective approach has a performance index ( $PI$ ) greater than 1, in which case substituting nanofluid for the base fluid in FPSCs is favorable. If the performance index is below 1, using the nanofluid in the system is not feasible.



### 3. Numerical Approach

#### 3.1. Geometric Configuration

A three-dimensional FPSC has been simulated in this study using the CFD package ANSYS Fluent [41] for analyzing the fluid flow behavior and the temperature distribution across the collector. The geometric details of FPSCs are extracted from the experimental work reported by [13] that the model was validated against. The computational domain of our modeling is shown in Figure 1, which comprised an aluminum absorber plate, two copper headers, and four connector riser tubes of the same material.

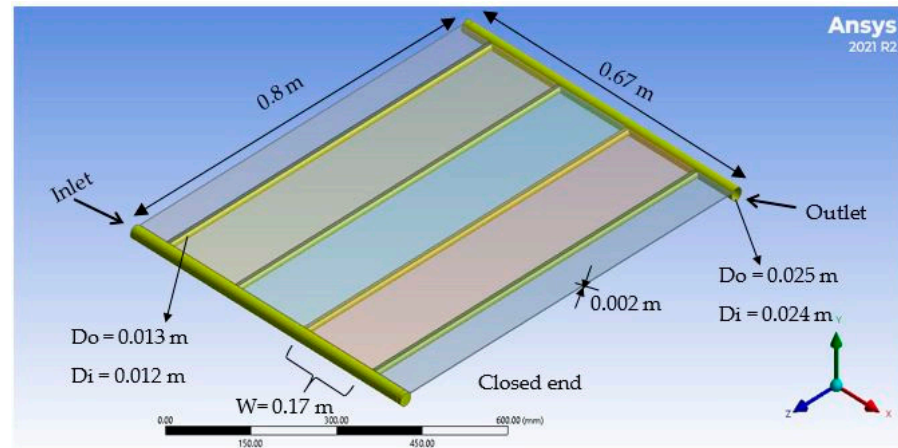


**Figure 1.** Geometric configuration of the computational model.

#### 3.2. Governing Equations

The numerical analysis is performed by coupling the Navier–Stokes and energy equations. The flow is taken to be steady, laminar, and incompressible. Furthermore, the nanofluid is considered to be single-phase. Under these considerations, the continuity, momentum, and energy equations in vector form are given as [42–46]:

Continuity:

$$\nabla \cdot (\rho_f \vec{v}_f) = 0 \quad (37)$$

Momentum:

$$\nabla \cdot (\rho_f \vec{v}_f \vec{v}_f) = -\nabla P + \nabla \cdot (\mu_f \nabla \vec{v}_f) + \rho \vec{g} \quad (38)$$

Energy:

$$\nabla \cdot (\rho C_p)_f \vec{v}_f T = \nabla \cdot (k_f \nabla T) \quad (39)$$

#### 3.3. Boundary Conditions

The required boundary conditions for numerical simulations of the investigated domain are presented in Table 1.

**Table 1.** Boundary conditions for the computational model.

Boundary Name	Conditions
Inlet	Uniform velocity and temperature
Absorber plate top	Uniform heat flux
Absorber plate side walls and bottom	Zero heat flux (i.e., adiabatic)
Header walls	Zero heat flux (i.e., adiabatic)
Interfaces (solid–solid and fluid–solid)	Thermally coupled
Outlet	Zero-gauge pressure

### 3.4. Mesh Independence Test

The mesh quality greatly influences the accuracy of results from CFD simulations. The outcomes are typically better, but the computation takes longer on average with finer meshes. The mesh configuration of the FPSC under study is shown in Figure 2. The absorber plate was split into different bodies for better mesh control, and higher-density structural mesh was taken into consideration close to the absorber plate and riser contact areas. The validity and consistency of the numerical results were examined using a mesh independence test. Four mesh densities were taken into consideration for a specific test case involving a base fluid (water) with a 0.0167 kg/s mass flow rate, 800 W/m<sup>2</sup> incident radiation, and 298 K ambient temperature. The collector outlet ( $T_o$ ) and the absorber plate temperature ( $T_p$ ) were both monitored for this test case. The inlet temperature ( $T_i$ ) was specified as 303 K. Table 2 provides a summary of the mesh independence test results and variations. A mesh size with 2,273,222 elements has been adopted for all the simulations to achieve a reasonable compromise between the results' accuracy and computational time.

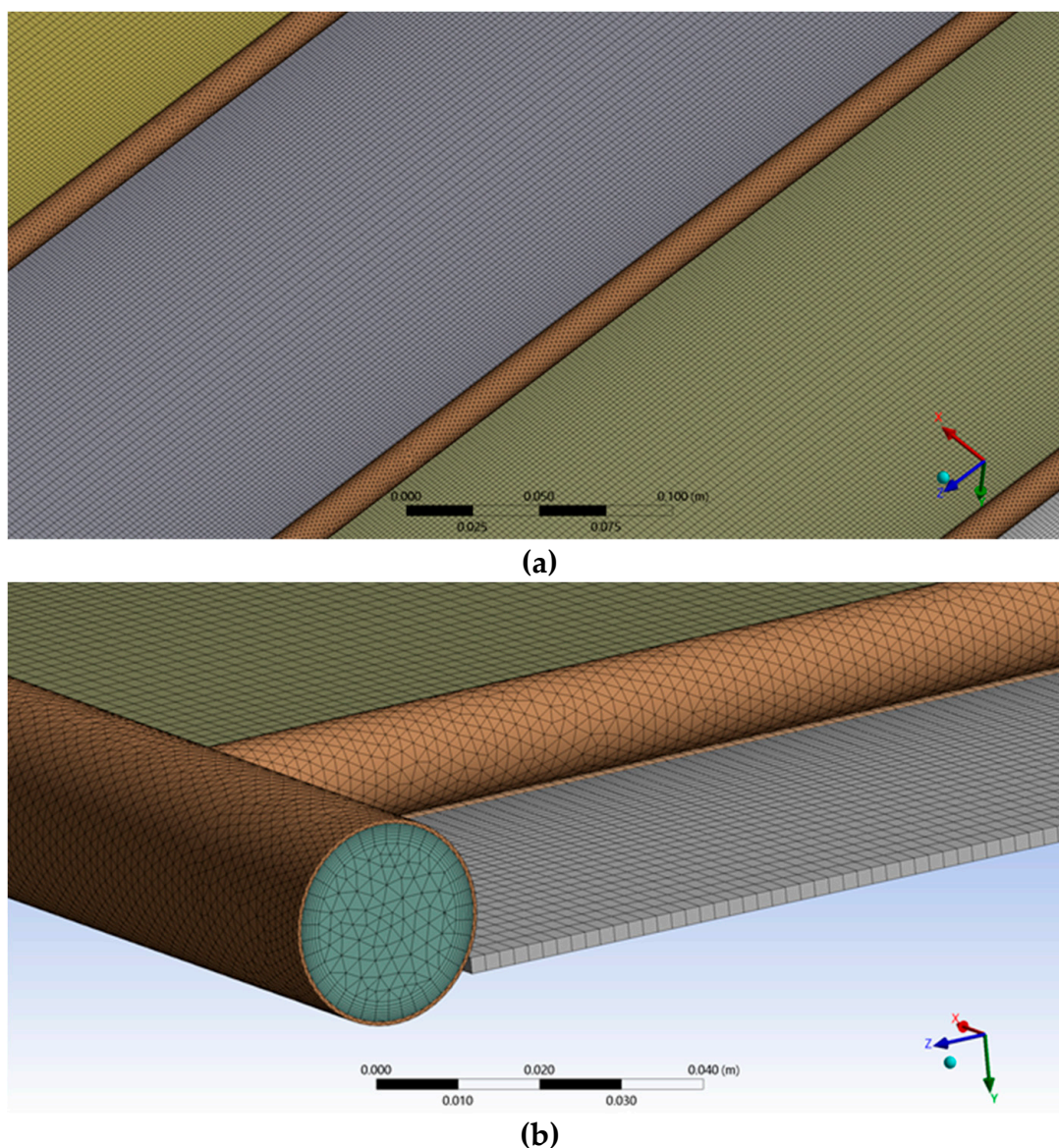


**Figure 2.** (a) Mesh layout of the computational model, and (b) a close-up of the mesh at the inlet header.

**Table 2.** Mesh independence test results and variations.

Number of Elements	$T_o$ (K)	Variation (%) in $T_o$	$T_p$ (K)	Variation (%) in $T_p$
739,646	307.165		311.236	
1,051,595	308.197	$3.35 \times 10^{-1}$	315.015	1.21
1,438,726	308.220	$7.46 \times 10^{-3}$	315.412	0.13
2,273,222	308.223	$9.73 \times 10^{-4}$	315.624	0.07
2,873,209	308.224	$3.24 \times 10^{-4}$	315.769	0.05

## 4. Input Data and Methodology

### 4.1. Input Data

The dimensions of the FPSC geometry and nanofluids' thermophysical properties are used as the input data for the numerical model. The input operating parameters also include the mass flow rate ( $\dot{m}$ ) and inlet temperature ( $T_i$ ), with respective ranges of 0.0167–0.05 kg/s and 303–333 K. Four volumetric fractions of nanoparticles—0.1%, 0.5%, 1%, and 2%—are used in the present investigation. Environmental factors such as wind speed, solar insolation, and ambient temperature are considered constant with values of 2.5 m/s, 800 W/m<sup>2</sup>, and 298 K, respectively.

### 4.2. Methodology

The methodology and iteration procedure followed in determining the performance of the FPSC is presented in Figure 3. Initially, a MATLAB program was used to determine the overall heat losses.  $T_{pm}$  must be known for calculating the overall heat loss coefficient ( $U_L$ ), as shown by Equations (2) and (3). Therefore, an initial arbitrary value of  $T_{pm}$  is chosen that is 10 K higher than the fluid inlet temperature ( $T_i$ ), as per the recommendation of [27]. Then,  $U_L$  and  $Q_u$  is determined from Equations (1) and (2). Following that, Equation (10) was used to determine the new  $T_{pm}$  value. The program then re-evaluates  $U_L$  and  $Q_u$  using the updated value of  $T_{pm}$ . This procedure is repeated in an iterative manner until the convergence criteria is satisfied. The total heat loss ( $Q_l$ ) per unit area of the FPSC is then estimated as follows:

$$Q_l = U_L(T_{pm} - T_a) \quad (40)$$

The heat flux ( $q'$ ) for the absorber plate is defined as:

$$q' = I(\tau\alpha)_e - Q_l \quad (41)$$

The next step is to apply heat flux into the ANSYS Fluent model, along with the appropriate boundary conditions to obtain the value of outlet temperature ( $T_o$ ), which is then used to determine energy efficiency ( $\eta_{en}$ ), exergy efficiency ( $\eta_{ex}$ ), and pressure drop ( $\Delta P$ ) of the FPSC. It is essential to mention that fluid flow was assumed to be uniform in MATLAB for estimating the heat losses; however, the actual mass flow rates and corresponding average velocities in risers can be obtained from the computational model (Fluent). Therefore, the average velocity in each riser is determined from the CFD model and is employed in the pressure drop calculations of the FPSC.

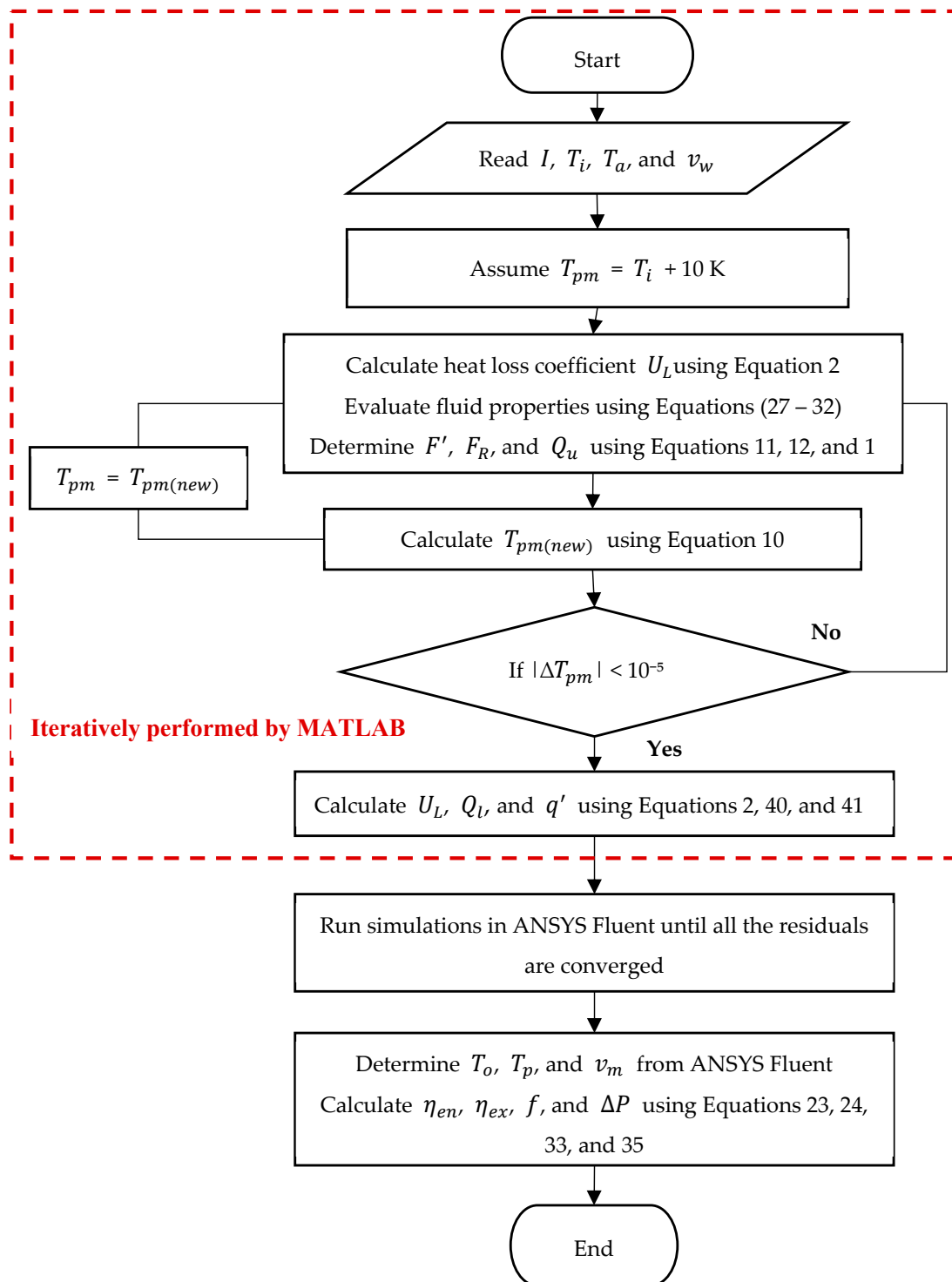


**Figure 3.** Flow chart of methodology and iteration procedure.

### 5. Model Validation

The validity of the present numerical model is tested by comparing the results of the absorber plate ( $T_p$ ) and collector outlet ( $T_o$ ) temperatures with the experimental findings of Jouybari et al. [13] for the case of nanofluid ( $\text{SiO}_2/\text{water}$ ) with 0.6% nanoparticle volumetric fraction and a 0.0333 kg/s (2 L/min) flow rate. The input variables for the CFD model are uniform inlet velocity ( $v_i$ ), uniform heat flux ( $q'$ ), inlet temperature ( $T_i$ ), and ambient temperature ( $T_a$ ). The physical properties of silica nanoparticles ( $\text{SiO}_2$ ) are taken from



the same publication and the experimental values of input parameters including  $I$ ,  $T_a$ ,  $T_i$ , and  $V_w$  were obtained from the authors. The comparison of numerical and experimental values of the collector outlet and absorber plate temperatures is shown in Figure 4. It is demonstrated that the values of  $T_o$  and  $T_p$  predicted by the simulation and the reported experimental findings accord well. The numerical results for  $T_o$  and  $T_p$  deviate from the experimental data by 0.13% and 0.91%, respectively.

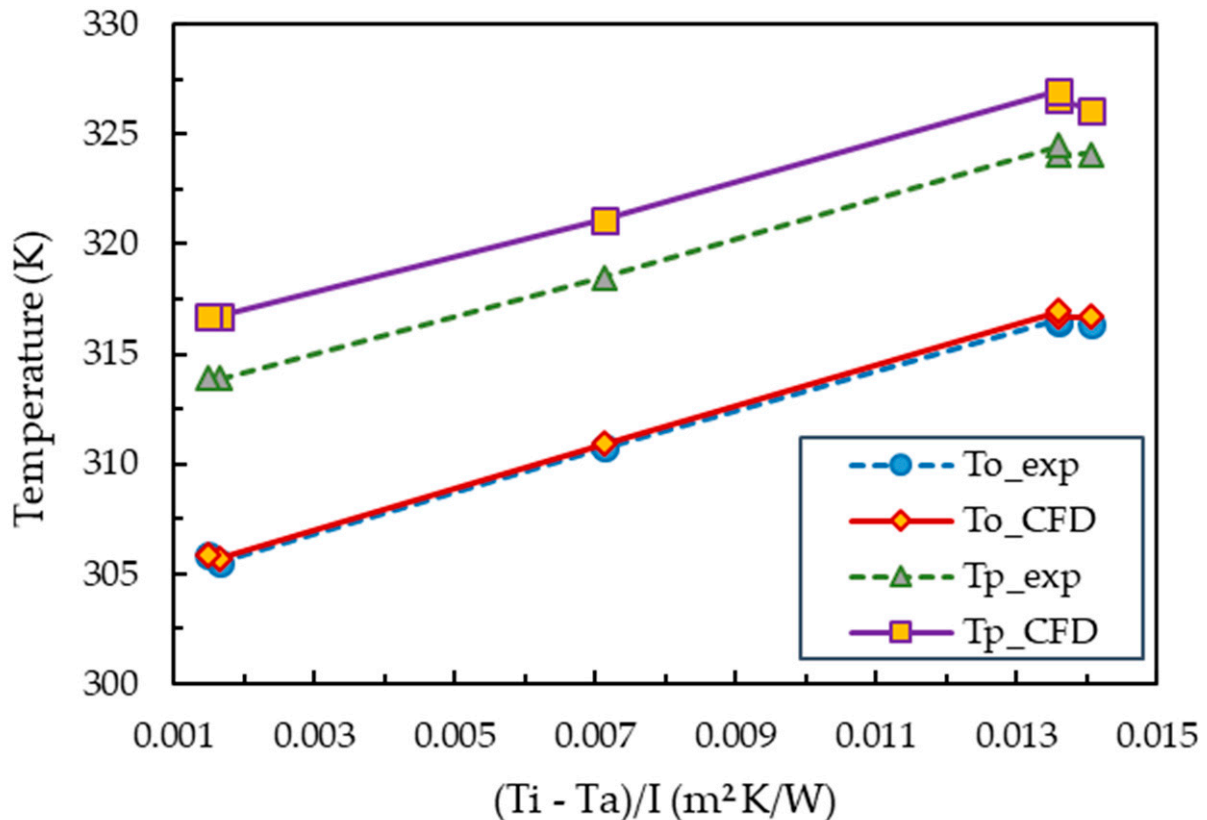


**Figure 4.** Validation of numerical results of absorber plate and collector outlet temperatures against the experimental results of [13].

## 6. Results and Discussions

A three-dimensional FPSC has been numerically modeled to investigate the effects of several influential parameters, namely nanoparticle volume fraction, mass flow rate, and inlet temperature on the thermo-hydraulic characteristics of FPSCs operating with  $\text{Fe}_3\text{O}_4$  water.

### 6.1. The Effect of Mass Flow Rate on Thermo-Hydraulic Characteristics of the FPSC

The effect of mass flow rate on FPSC's energy efficiency is shown in Figure 5. It can be seen that energy efficiency rises with the rise in flow rate. This effect can be explained through an important fact of reducing thermal resistance with rising fluid velocity. As a result, heat transfer coefficients are improved, which raises energy efficiency as the mass flow rate goes up. However, this will be accompanied by higher fluid friction and thus higher pressure drop across the collector due to the direct relationship between pressure drop and fluid's velocity based on Equation (33). The rise in energy efficiency with increasing flow rate can also be explained from another perspective; since there is less time to exchange heat between the fluid and tubes at high flow rates, the collector's outlet temperature reduces. As a result, the temperature difference of working fluids would reduce between the inlet and outlet. This will lead to lower thermal losses because of the collector's lower average temperature, and an enhancement in useful energy gain.

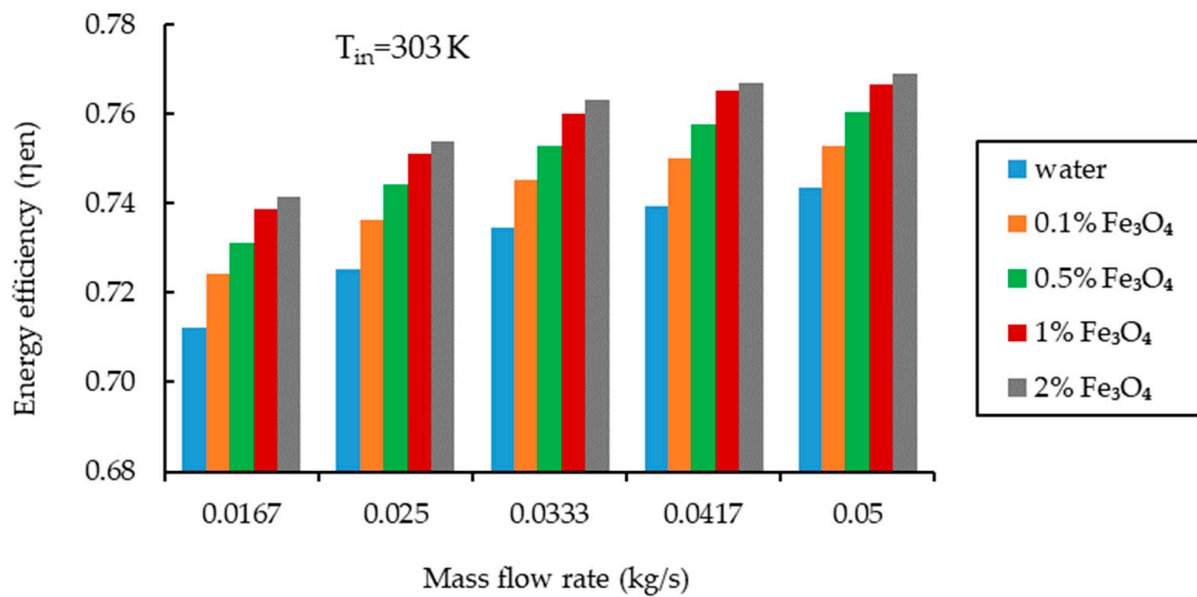


Figure 5. The effect of mass flow rate on the energy efficiency of FPSCs.

Furthermore, the addition of Fe<sub>3</sub>O<sub>4</sub> nanoparticles improves energy efficiency, which appraises the nanofluid's positive influence on FPSC's thermal performance. This is due to an increment in outlet temperature and a drop in absorber plate mean temperature with the increased particle volume fraction, as illustrated in Figure 6. Thermal losses will be reduced as the absorber plate temperature drops, and energy efficiency will increase. When compared to water, the maximum increase in energy efficiency is observed at 0.0167 kg/s, which is 1.68%, 2.64%, 3.70%, and 4.28% at 0.1%, 0.5%, 1%, and 2% volumetric fraction, respectively.

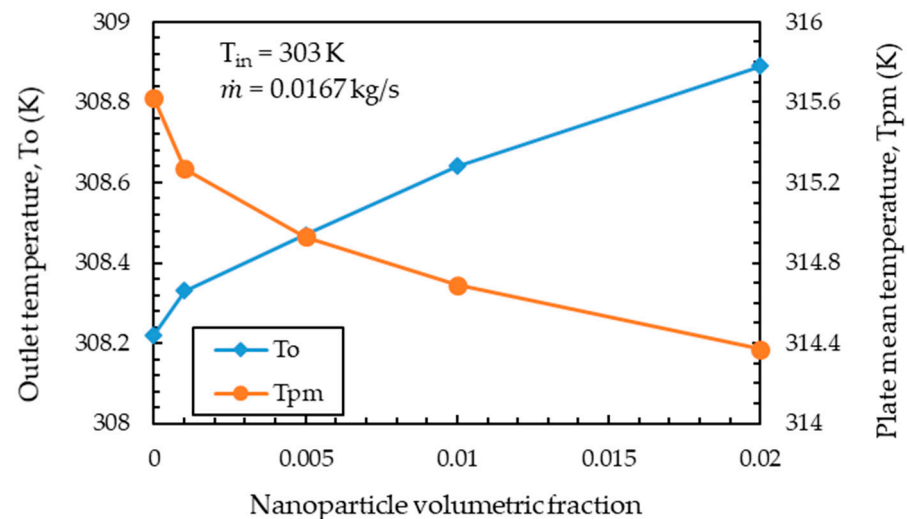
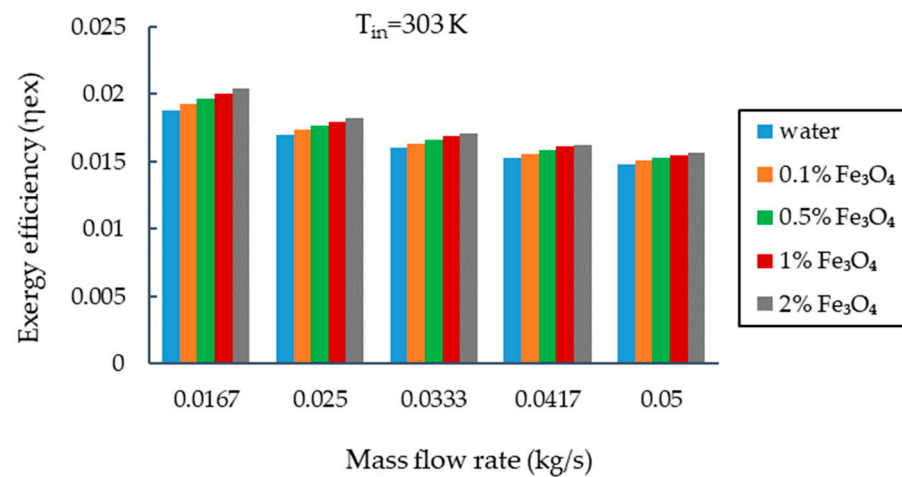


Figure 6. The influence of nanoparticle volume fraction on outlet temperature and absorber plate mean temperature.

Exergy efficiency, in contrast to energy efficiency, performs better at low flow rates (Figure 7). The collector's exergy output is found to decline with the rise in flow rate because of a reduction in outlet temperature. Consequently, less useful work is obtained from the system with a rise in mass flow rate. With 0.1%, 0.5%, 1%, and 2% particle fractions, respectively, the improvement in exergy efficiency is found to be 2.43%, 4.33%, 6.56%, and 8.90%.



**Figure 7.** The effect of mass flow rate on exergy efficiency of FPSCs.

Another crucial factor to consider when evaluating the performance of an FPSC is the convective heat transfer coefficient. Figure 8 demonstrates the contribution of mass flow rate in affecting the convective heat transfer coefficient. It appears to rise linearly with the mass flow rate and nanoparticles further improve it. This is due to the direct relationship between  $h_f$  and fluid's thermal conductivity ( $k_f$ ) based on Equation (14). The heat transfer coefficient improved by 6.92%, 12.90%, 18.46%, and 27.31% using Fe<sub>3</sub>O<sub>4</sub> with 0.1%, 0.5%, 1%, and 2% volumetric fractions, respectively.

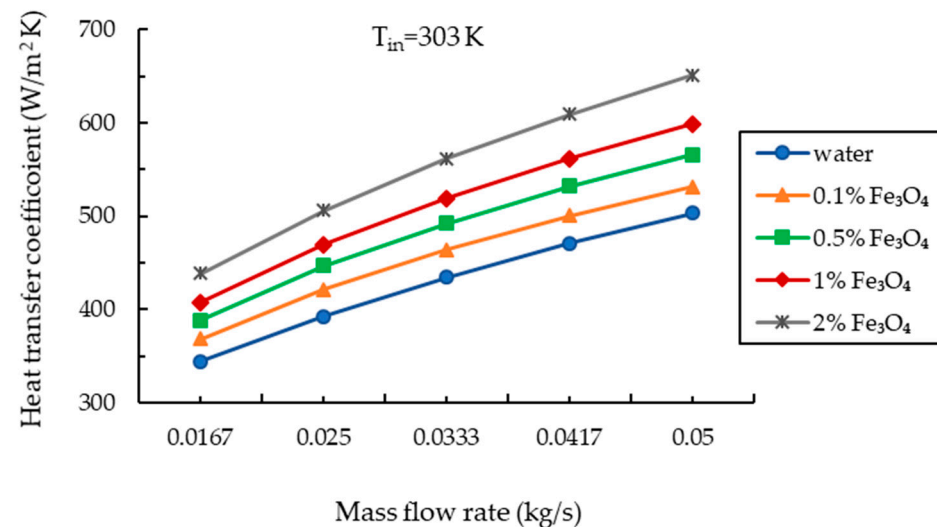


**Figure 8.** The effect of mass flow rate on convective heat transfer coefficient of FPSCs.

Figure 9 demonstrates that nanofluids have higher friction factor and pressure drop values than water, particularly above 0.5% nanoparticle fraction. At 0.1, 0.5, 1, and 2 vol.%, respectively, nanofluids increased the pressure drop across the collector by 0.38%, 1.98%, 3.96%, and 7.93%, and the friction factor by 0.90%, 3.60%, 6.31%, and 13.51%. This penalty results from the fluid's increased dynamic viscosity because of nanoparticles, which lowers the Reynolds number according to Equation (19) if the mass flow rate remains constant. This results in a higher friction factor because of its inverse relationship with the Reynolds number and, therefore, a higher pressure drop across the collector. Additionally, it is found that at a fixed volume fraction, pressure drop gradually rises as the flow rate increases. The reason for this is that higher fluid velocities lead to higher velocity gradients in the risers and, consequently, higher viscous losses. On the other hand, the friction factor considerably declines with the rising flow rate.



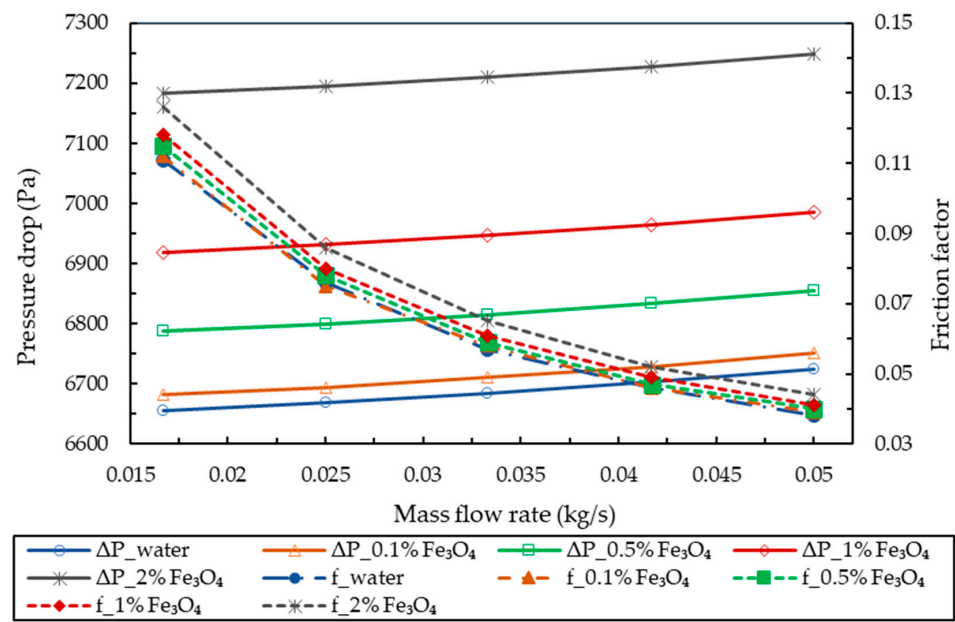


Figure 9. The effect of mass flow rate on friction factor and pressure drop of FPSCs.

### 6.2. The Effect of Inlet Temperature on Thermo-Hydraulic Characteristics of FPSCs

The variation of energy and exergy efficiencies with inlet temperature is seen in Figure 10. Energy efficiency is seen to decline linearly as inlet temperature increases. This may be related to the increased heat losses from the collector’s absorber. The absorber plate’s mean temperature increases together with the inlet temperature, implying that there is more thermal energy available for losses through conduction, convection, and radiation as the inlet temperature goes up. This results in a higher value of  $U_L$ ; therefore. Lower heat flux is available to convert into useful energy.

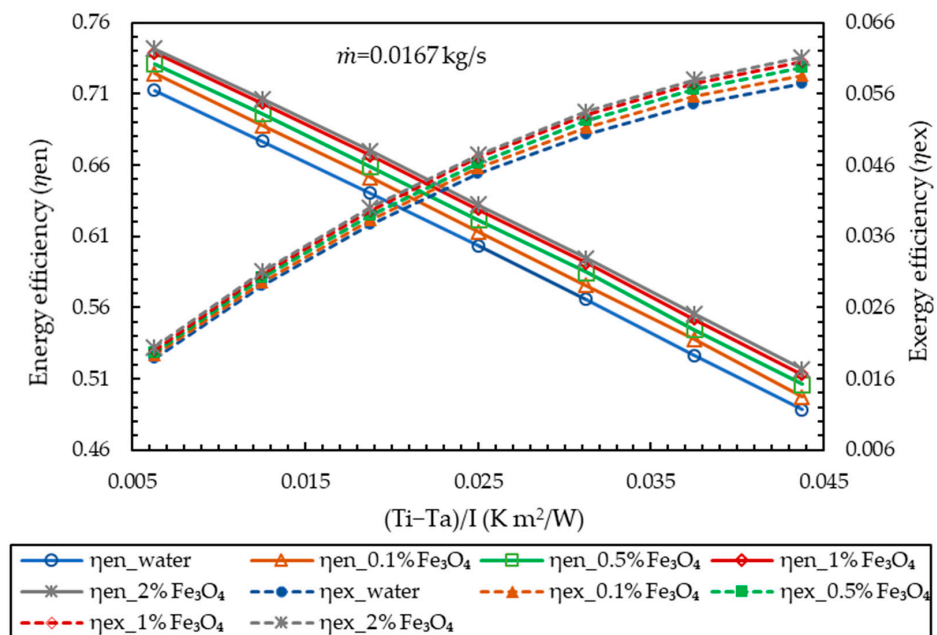


Figure 10. The effect of inlet temperature on energy and exergy efficiencies of FPSCs.

On the other hand, the exergy efficiency improves at high inlet temperatures. This is because exergy loss decreases with rising inlet temperature and absorber plate temperature. As stated by [47], the difference in temperature between the sun and absorber plate is the

main reason for this exergy loss. In accordance, as the absorber plate temperature goes up, the temperature difference will be reduced. This helps in reducing exergy loss and, ultimately, augments the collector’s useful exergy. Additionally, Figure 10 indicates that for the investigated range of inlet temperature, nanoparticles have a favorable effect on both efficiencies. Utilizing Fe<sub>3</sub>O<sub>4</sub> nanoparticles at 0.1%, 0.5%, 1%, and 2%, respectively, an increase in exergy efficiency of 2.43%, 4.33%, 6.56%, and 8.90% is obtained.

The inlet temperature also influences the convective heat transfer. In Figure 11, at 303 K inlet temperature, the increment in the volume percentage of Fe<sub>3</sub>O<sub>4</sub> from 0.1% to 2% provides an improvement in coefficient heat transfer of 6.30% to 26.93%, compared to pure water. This enhancement is seen to increase further with temperature, especially for higher volume fractions (1% and 2%), as higher temperatures raise the nanofluid’s thermal conductivity. Noteworthy is that higher temperatures augment the convective heat transfer coefficient while reducing the overall energy efficiency of FPSC. This implies that the losses from the collector absorber outweigh the temperature’s positive impact on heat transfer. Therefore, at high temperatures, the collector yields less amount of useful energy. Furthermore, in Figure 12, there has been a downward trend in both the friction factor and pressure drop with increasing temperature. This is because higher temperatures lead to a reduction in density and effective viscosity, which lowers viscous losses.

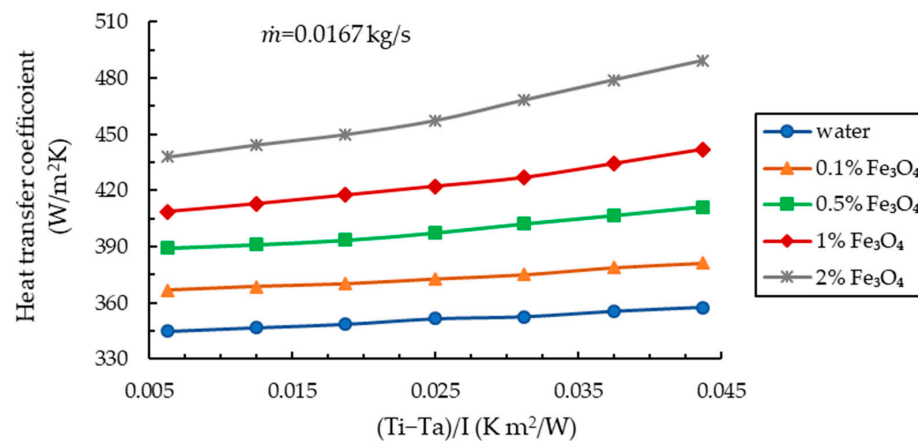


Figure 11. The effect of inlet temperature on convective heat transfer coefficient of FPSCs.

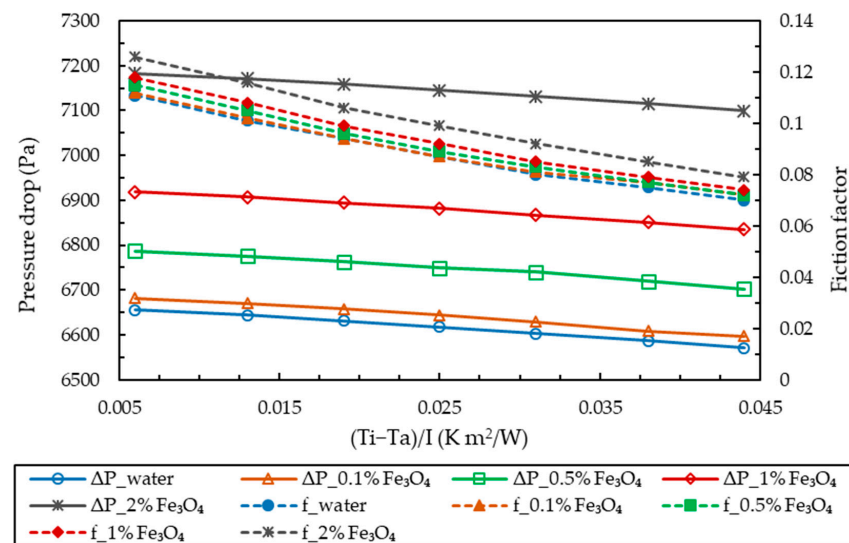
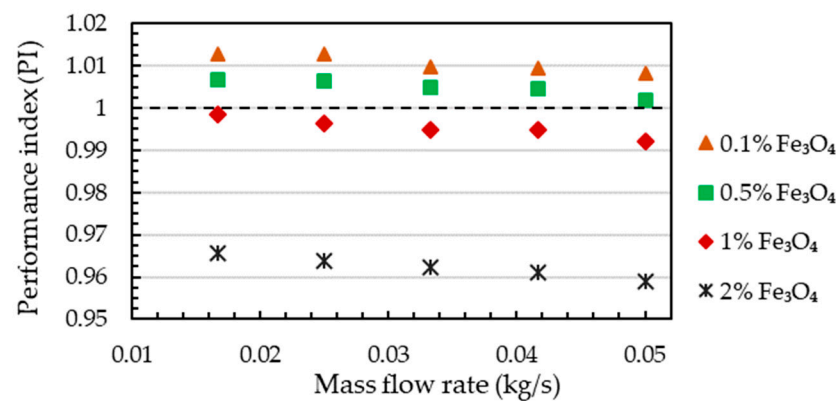


Figure 12. The effect of inlet temperature on friction factor and pressure drop of FPSCs.

### 6.3. Performance Index (PI)

To assess the effectiveness of magnetite ( $\text{Fe}_3\text{O}_4$ ) nanofluid as solar thermal fluid in FPSCs, the performance index is determined for different volume fractions. Figure 13 illustrates the variation of the performance index of  $\text{Fe}_3\text{O}_4$  water nanofluid with flow rate. As can be observed, performance index values for 0.1% and 0.5% volumetric fractions are greater than 1, regardless of the flow rate. However, the values for 1% and 2% volume fractions are less than 1. Additionally, *PI* values fall when the mass flow rate is augmented. Numerical findings lead to the conclusion that using  $\text{Fe}_3\text{O}_4$  water nanofluid at volume fractions greater than 0.5% is not a practically viable option because the rise in pressure drop is more significant than the improvement in energy efficiency.



**Figure 13.** Performance index variation with flow rate.

### 6.4. Temperature and Flow Distribution across FPSCs

Figure 14 shows the distribution of temperature throughout the fluid domain. The heat picked up by the fluid as it passes through the headers and risers can be visualized through the temperature distribution. Moreover, the flow distribution in the headers and risers of the collector is depicted in Figure 15. Since the nanofluid in the current study is assumed to be a single-phase fluid having modified properties, the flow behavior of water and nanofluid is found to be similar, with the exception of magnitudes of average velocities in risers and headers. Because of the similarity in the flow behavior, only one set of vector plots with an optimum volume fraction of nanoparticles (0.5%) is shown in the figure.

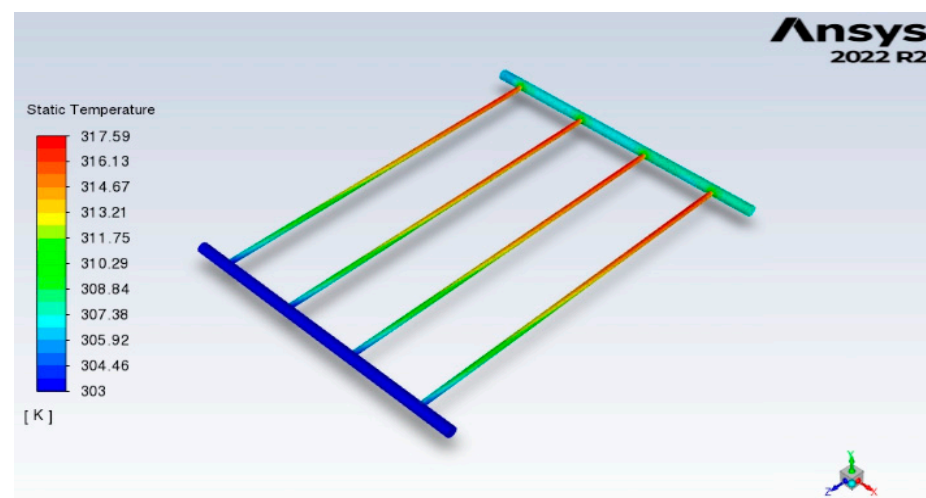


**Figure 14.** Temperature distribution of the fluid domain for 0.5% volume fraction, 0.0167 kg/s flow rate, and 303 K inlet temperature.

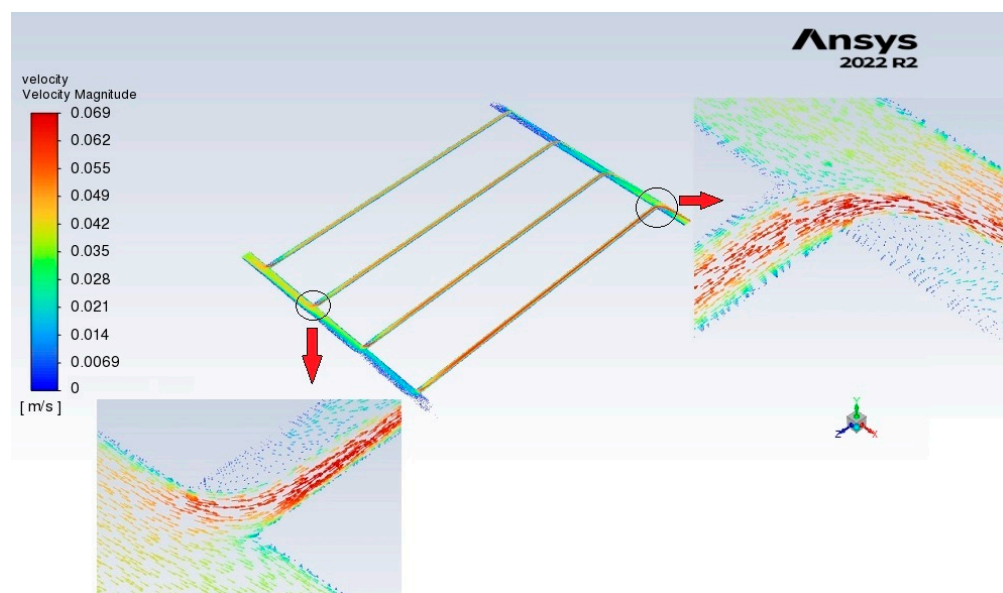


**Figure 15.** The flow pattern inside the collector's risers and headers for 0.5% volume fraction, 303 K inlet temperature, and 0.0167 kg/s mass flow rate.

## 7. Conclusions

This study numerically investigated the potential of magnetite nanofluid ( $\text{Fe}_3\text{O}_4$  water) in the FPSC. The combined methodology of MATLAB and CFD modeling was validated against the published literature and it was further employed for investigating the influence of a number of operational parameters, including nanoparticle volumetric fraction, mass flow rate, and inlet temperature on the thermo-hydraulic characteristics of FPSCs. These characteristics include energy efficiency, exergy efficiency, convection heat transfer, friction factor, and pressure drop. The numerical results demonstrated that regardless of the fluid type, energy efficiency rises with increasing flow rate and reducing inlet temperature. In addition, at higher inlet temperatures, energy efficiency falls while exergy efficiency increases. An enhancement of 4.28% and 8.90% was found in energy and exergy efficiencies, respectively.

Overall, the maximum enhancement in FPSC's thermal performance was found using a higher volume fraction of  $\text{Fe}_3\text{O}_4$  (i.e., 2%), but at the cost of increased friction factor and pressure drop, which were 13.51% and 7.93% higher, respectively, than water. The performance index is in general above 1 for a nanoparticle volume fraction  $\leq 0.5\%$ . Based on the outcomes, 0.5% is considered as an optimum volume fraction which presented an improvement in heat transfer coefficient, collector's energy, and exergy efficiencies of 12.90%, 2.64%, and 4.33%, respectively, with a negligible penalty in pressure drop.

**Author Contributions:** Conceptualization, M.S., G.L. and D.M.; methodology, M.S.; software, M.S. and W.J.; validation, M.S.; formal analysis, M.S.; investigation, M.S.; data curation, M.S.; writing—original draft preparation, M.S.; writing—review and editing, M.S., M.F., W.J., G.L. and D.M.; supervision, G.L. and D.M. All authors have read and agreed to the published version of the manuscript.

**Funding:** This research received no external funding.

**Institutional Review Board Statement:** Not applicable.

**Informed Consent Statement:** Not applicable.

**Data Availability Statement:** Not applicable.

**Conflicts of Interest:** The authors declare no conflict of interest.

## Nomenclature

$A_c$	Collector area ( $m^2$ )
$C_{bond}$	Bond conductance ( $W/(m \cdot K)$ )
$D$	Diameter of tube (m)
$f$	Friction factor
$h$	Convective heat transfer coefficient ( $W/(m^2 \cdot K)$ )
$I$	Incident solar radiation ( $W/m^2$ )
$L_r$	Riser tube length (m)
$Nu$	Nusselt number
$Pr$	Prandtl number
$Pe$	Peclet number
$Re$	Reynolds number
$T$	Temperature (K)
$U_L$	Overall heat loss coefficient ( $W/(m^2 \cdot K)$ )
$W$	Riser tube spacing (m)
Greek symbols	
$\alpha$	Thermal diffusivity ( $m^2/s$ )
$\beta$	Collector tilt angle (degree)
$\mu$	Dynamic viscosity (kg/m s)
$\rho$	Density (kg/m <sup>3</sup> )
$\sigma$	Stefan–Boltzmann constant ( $5.67 \times 10^{-8} W/(m^2 K^4)$ )
$\varepsilon$	Emissivity
$\delta$	Thickness (m)
$\phi$	Nanoparticle volume fraction (%)
Subscripts	
a	Ambient
b	Bottom
bf	Base fluid
e	Edge
f	Fluid
i	Inlet
ins	Insulation
nf	Nanofluid
np	Nanoparticle
o	Outlet
pm	Plate mean
t	Top
Abbreviations	
FPSC	Flat-plate solar collector
ETC	Evacuated tube collector
MWCNT	Multi-wall carbon nanotubes
PI	Performance index

## References

1. IEA. Heating, IEA, Paris. 2022. Available online: <https://www.iea.org/reports/heating> (accessed on 7 January 2023).
2. Weiss, W.; Spörk-Dür, M. Solar Heat World. Global Market Development and Trends 2021. Available online: <https://www.iea-shc.org/Data/Sites/1/publications/Solar-Heat-Worldwide-2021.pdf> (accessed on 7 January 2023).
3. Wang, Z.; Yang, W.; Qiu, F.; Zhang, X.; Zhao, X. Solar water heating: From theory, application, marketing and research. *Renew. Sustain. Energy Rev.* **2015**, *41*, 68–84. [[CrossRef](#)]
4. Alawi, O.A.; Kamar, H.M.; Mallah, A.; Mohammed, H.A.; Kazi, S.; Sidik, N.A.C.; Najafi, G. Nanofluids for flat plate solar collectors: Fundamentals and applications. *J. Clean. Prod.* **2020**, *291*, 125725. [[CrossRef](#)]
5. Choi, S.U.S. Enhancing thermal conductivity of fluids with nanoparticles. *Am. Soc. Mech. Eng. Fluids Eng. Div. FED* **1995**, *231*, 99–105.
6. Godson, L.; Raja, B.; Lal, D.M.; Wongwises, S. Enhancement of heat transfer using nanofluids—An overview. *Renew. Sustain. Energy Rev.* **2010**, *14*, 629–641. [[CrossRef](#)]
7. He, Q.; Zeng, S.; Wang, S. Experimental investigation on the efficiency of flat-plate solar collectors with nanofluids. *Appl. Therm. Eng.* **2015**, *88*, 165–171. [[CrossRef](#)]



8. Moghadam, A.J.; Farzane-Gord, M.; Sajadi, M.; Hoseyn-Zadeh, M. Effects of CuO/water nanofluid on the efficiency of a flat-plate solar collector. *Exp. Therm. Fluid Sci.* **2014**, *58*, 9–14. [[CrossRef](#)]
9. Genc, A.M.; Ezan, M.A.; Turgut, A. Thermal performance of a nanofluid-based flat plate solar collector: A transient numerical study. *Appl. Therm. Eng.* **2018**, *130*, 395–407. [[CrossRef](#)]
10. Sharafeldin, M.A.; Gróf, G.; Mahian, O. Experimental study on the performance of a flat-plate collector using WO<sub>3</sub>/Water nanofluids. *Energy* **2017**, *141*, 2436–2444. [[CrossRef](#)]
11. Sharafeldin, M.; Gróf, G. Experimental investigation of flat plate solar collector using CeO<sub>2</sub>-water nanofluid. *Energy Convers. Manag.* **2018**, *155*, 32–41. [[CrossRef](#)]
12. Sarsam, W.; Kazi, S.; Badarudin, A. Thermal performance of a flat-plate solar collector using aqueous colloidal dispersions of graphene nanoplatelets with different specific surface areas. *Appl. Therm. Eng.* **2020**, *172*, 115142. [[CrossRef](#)]
13. Jouybari, H.J.; Nimvari, M.E.; Saedodin, S. Thermal performance evaluation of a nanofluid-based flat-plate solar collector: An experimental study and analytical modeling. *J. Therm. Anal. Calorim.* **2019**, *137*, 1757–1774. [[CrossRef](#)]
14. Hawwash, A.; Rahman, A.K.A.; Nada, S.; Ookawara, S. Numerical Investigation and Experimental Verification of Performance Enhancement of Flat Plate Solar Collector Using Nanofluids. *Appl. Therm. Eng.* **2018**, *130*, 363–374. [[CrossRef](#)]
15. Tong, Y.; Chi, X.; Kang, W.; Cho, H. Comparative investigation of efficiency sensitivity in a flat plate solar collector according to nanofluids. *Appl. Therm. Eng.* **2020**, *174*, 115346. [[CrossRef](#)]
16. Hepbasli, A. A key review on exergetic analysis and assessment of renewable energy resources for a sustainable future. *Renew. Sustain. Energy Rev.* **2008**, *12*, 593–661. [[CrossRef](#)]
17. Verma, S.K.; Tiwari, A.K.; Chauhan, D.S. Performance augmentation in flat plate solar collector using MgO/water nanofluid. *Energy Convers. Manag.* **2016**, *124*, 607–617. [[CrossRef](#)]
18. Verma, S.K.; Tiwari, A.K.; Chauhan, D.S. Experimental evaluation of flat plate solar collector using nanofluids. *Energy Convers. Manag.* **2017**, *134*, 103–115. [[CrossRef](#)]
19. Tong, Y.; Lee, H.; Kang, W.; Cho, H. Energy and exergy comparison of a flat-plate solar collector using water, Al<sub>2</sub>O<sub>3</sub> nanofluid, and CuO nanofluid. *Appl. Therm. Eng.* **2019**, *159*, 113959. [[CrossRef](#)]
20. Okonkwo, E.C.; Wole-Osho, I.; Kavaz, D.; Abid, M.; Al-Ansari, T. Thermodynamic evaluation and optimization of a flat plate collector operating with alumina and iron mono and hybrid nanofluids. *Sustain. Energy Technol. Assess.* **2020**, *37*, 100636. [[CrossRef](#)]
21. Moghadam, M.C.; Edalatpour, M.; Solano, J.P. Numerical Study on Conjugated Laminar Mixed Convection of Alumina/Water Nanofluid Flow, Heat Transfer, and Entropy Generation Within a Tube-on-Sheet Flat Plate Solar Collector. *J. Sol. Energy Eng.* **2017**, *139*, 041011. [[CrossRef](#)]
22. Mostafizur, R.; Rasul, M.; Nabi, M. Energy and Exergy Analyses of a Flat Plate Solar Collector Using Various Nanofluids: An Analytical Approach. *Energies* **2021**, *14*, 4305. [[CrossRef](#)]
23. Faizal, M.; Saidur, R.; Mekhilef, S.; Alim, M. Energy, economic and environmental analysis of metal oxides nanofluid for flat-plate solar collector. *Energy Convers. Manag.* **2013**, *76*, 162–168. [[CrossRef](#)]
24. Zayed, M.; Zhao, J.; Du, Y.; Kabeel, A.; Shalaby, S. Factors affecting the thermal performance of the flat plate solar collector using nanofluids: A review. *Sol. Energy* **2019**, *182*, 382–396. [[CrossRef](#)]
25. Akram, N.; Sadri, R.; Kazi, S.N.; Zubir, M.N.M.; Ridha, M.; Ahmed, W.; Soudagar, M.E.M.; Arzpeyma, M. *A Comprehensive Review on Nanofluid Operated Solar Flat Plate Collectors*; Springer International Publishing: Berlin/Heidelberg, Germany, 2020. [[CrossRef](#)]
26. Wole-Osho, I.; Okonkwo, E.C.; Abbasoglu, S.; Kavaz, D. *Nanofluids in Solar Thermal Collectors: Review and Limitations*; Springer: Berlin/Heidelberg, Germany, 2020. [[CrossRef](#)]
27. Duffie, J.A.; Beckman, W.A. *Solar Engineering of Thermal Processes*, 4th ed.; John Wiley & Sons, Inc.: Hoboken, NJ, USA, 2013.
28. Jiandong, Z.; Hanzhong, T.; Susu, C. Numerical simulation for structural parameters of flat-plate solar collector. *Sol. Energy* **2015**, *117*, 192–202. [[CrossRef](#)]
29. Sartori, E. Convection coefficient equations for forced air flow over flat surfaces. *Sol. Energy* **2006**, *80*, 1063–1071. [[CrossRef](#)]
30. Holman, V. Introduction. *Vis. Resour.* **1999**, *15*, ix–x. [[CrossRef](#)]
31. Yimin, X.; Qiang, L. Convective heat transfer and flow characteristics of Cu-water nanofluid. *Convect. Heat Transf.* **2002**, *45*, 408–416.
32. Bellos, E.; Tzivanidis, C.; Daniil, I.; Antonopoulos, K.A. The impact of internal longitudinal fins in parabolic trough collectors operating with gases. *Energy Convers. Manag.* **2017**, *135*, 35–54. [[CrossRef](#)]
33. Rodríguez, E.; Cardemil, J.M.; Starke, A.R.; Escobar, R. Modelling the Exergy of Solar Radiation: A Review. *Energies* **2022**, *15*, 1477. [[CrossRef](#)]
34. Petela, R. Exergy of undiluted thermal radiation. *Sol. Energy* **2003**, *74*, 469–488. [[CrossRef](#)]
35. Pak, B.C.; Cho, Y.I. Hydrodynamic and heat transfer study of dispersed fluids with submicron metallic oxide particles. *Exp. Heat Transf.* **1998**, *11*, 151–170. [[CrossRef](#)]
36. Xuan, Y.; Roetzel, W. Conceptions for heat transfer correlation of nanofluids. *Int. J. Heat Mass Transf.* **2000**, *43*, 3701–3707. [[CrossRef](#)]
37. Corcione, M. Empirical correlating equations for predicting the effective thermal conductivity and dynamic viscosity of nanofluids. *Energy Convers. Manag.* **2011**, *52*, 789–793. [[CrossRef](#)]

38. Gertzog, K.; Pnevmatikakis, S.; Caouris, Y. Experimental and numerical study of heat transfer phenomena, inside a flat-plate integrated collector storage solar water heater (ICSSWH), with indirect heat withdrawal. *Energy Convers. Manag.* **2008**, *49*, 3104–3115. [[CrossRef](#)]
39. Mahian, O.; Kianifar, A.; Sahin, A.Z.; Wongwises, S. Entropy generation during Al<sub>2</sub>O<sub>3</sub>/water nanofluid flow in a solar collector: Effects of tube roughness, nanoparticle size, and different thermophysical models. *Int. J. Heat Mass Transf.* **2014**, *78*, 64–75. [[CrossRef](#)]
40. Cimbala, J.M.; Cengel, Y.A. *Fluid Mechanics: Fundamentals and Applications*, 4th ed.; McGraw-Hill Higher Education: New York, NY, USA, 2018.
41. Canonsburg, T.D. *ANSYS Fluent Theory Guide*; ANSYS Inc.: Washington County, PA, USA, 2013.
42. Vanaki, S.; Ganesan, P.; Mohammed, H. Numerical study of convective heat transfer of nanofluids: A review. *Renew. Sustain. Energy Rev.* **2016**, *54*, 1212–1239. [[CrossRef](#)]
43. Albojamal, A.; Vafai, K. Analysis of single phase, discrete and mixture models, in predicting nanofluid transport. *Int. J. Heat Mass Transf.* **2017**, *114*, 225–237. [[CrossRef](#)]
44. Moraveji, M.K.; Ardehali, R.M. CFD modeling (comparing single and two-phase approaches) on thermal performance of Al<sub>2</sub>O<sub>3</sub>/water nanofluid in mini-channel heat sink. *Int. Commun. Heat Mass Transf.* **2013**, *44*, 157–164. [[CrossRef](#)]
45. Atashafrooz, M.; Sajjadi, H.; Delouei, A.A. Simulation of combined convective-radiative heat transfer of hybrid nanofluid flow inside an open trapezoidal enclosure considering the magnetic force impacts. *J. Magn. Magn. Mater.* **2023**, *567*, 170354. [[CrossRef](#)]
46. Atashafrooz, M.; Sajjadi, H.; Delouei, A.A. Interacting influences of Lorentz force and bleeding on the hydrothermal behaviors of nanofluid flow in a trapezoidal recess with the second law of thermodynamics analysis. *Int. Commun. Heat Mass Transf.* **2019**, *110*, 104411. [[CrossRef](#)]
47. Gunjo, D.G.; Mahanta, P.; Robi, P. CFD and experimental investigation of flat plate solar water heating system under steady state condition. *Renew. Energy* **2017**, *106*, 24–36. [[CrossRef](#)]

**Disclaimer/Publisher's Note:** The statements, opinions and data contained in all publications are solely those of the individual author(s) and contributor(s) and not of MDPI and/or the editor(s). MDPI and/or the editor(s) disclaim responsibility for any injury to people or property resulting from any ideas, methods, instructions or products referred to in the content.